Delft University of Technology

A global statistical assessment of designing silicon-based solar cells for geographical markets

Ziar, Hesan

DOI
10.1016/j.joule.2024.02.023

Publication date
2024

Document Version
Final published version

Published in
Joule

Citation (APA)
Ziar, H. (2024). A global statistical assessment of designing silicon-based solar cells for geographical markets. *Joule*, *8*(6), 1667-1690. https://doi.org/10.1016/j.joule.2024.02.023

Important note
To cite this publication, please use the final published version (if applicable).
Please check the document version above.

Copyright
Other than for strictly personal use, it is not permitted to download, forward or distribute the text or part of it, without the consent of the author(s) and/or copyright holder(s), unless the work is under an open content license such as Creative Commons.

Takedown policy
Please contact us and provide details if you believe this document breaches copyrights.
We will remove access to the work immediately and investigate your claim.

This work is downloaded from Delft University of Technology.
For technical reasons the number of authors shown on this cover page is limited to a maximum of 10.

Green Open Access added to TU Delft Institutional Repository

'You share, we take care!' - Taverne project

https://www.openaccess.nl/en/you-share-we-take-care

Otherwise as indicated in the copyright section: the publisher
is the copyright holder of this work and the author uses the
Dutch legislation to make this work public.

Joule

CellPress

Article

A global statistical assessment of designing silicon-based solar cells for geographical markets

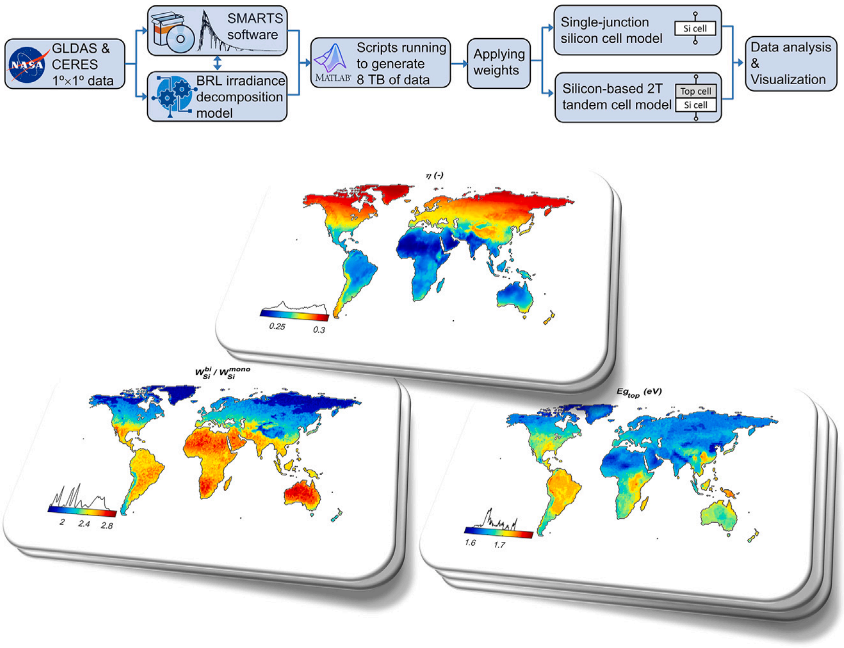

This work optimizes the design of single- and double-junction crystalline silicon-based solar cells for more than 15,000 terrestrial locations. The sheer breadth of the simulation, coupled with the vast dataset it generated, makes it possible to extract statistically robust conclusions regarding the pivotal design parameters of PV cells, with a particular emphasis on silicon wafers. The result underlines the critical importance of tailoring solar cell design to distinct geographical contexts, which unlocks a staggering potential for polysilicon savings.

Hesan Ziar

h.ziar@tudelft.nl

Highlights

The design of single- and double-junction Si-based solar cells is mapped globally

An optimum Si cell in Australia should be 50% thinner than its counterpart in Europe

The reevaluated theoretical efficiency limit of X-on-Si tandem cells is 42.8%

Designing solar cells based on geographical markets is a resource-efficient practice

Ziar, Joule 8, 1667–1690
June 19, 2024 © 2024 Elsevier Inc.
https://doi.org/10.1016/j.joule.2024.02.023

Joule

CellPress

Article

A global statistical assessment of designing silicon-based solar cells for geographical markets

Hesan Ziar[1,2,*]

SUMMARY

Here, we first visualize the achievable global efficiency for single-junction crystalline silicon cells and demonstrate how different regional markets have radically varied requirements for Si wafer thickness and injection level. Our findings showed that 219 g/kW of polysilicon can be conserved while producing slightly more electricity when c- Si cells are manufactured based on the global geographical market instead of standard test conditions. Then, we investigate the bifacial silicon cell and show that its optimal wafer thickness should be 1.67–2.89 times thicker than its monofacial counterpart, depending on the geographical region. Further, we study a double-junction two-terminal Si-based cell, reevaluate its theoretical limit as 42.8%, and illustrate that globally, tandem cells' efficiency will only be slightly decreased when significantly reducing the bottom cell Si wafer thickness ($-0.3\%/\mathrm{mm}$). The outcomes of this study offer a blueprint to strategically design solar cells for target geographic markets, ensuring the conservation of substantial polysilicon volumes.

INTRODUCTION

Solar photovoltaics (PV) has recently entered the so-called Terawatt era,[1] indicating that the cumulative PV power installed all over the globe has surpassed 1 TW. Swanson's PV learning curve also continued to decline, making PV installations the lowest-cost option for electricity generation.[2] Data from the past two decades show that the PV industry is prepared to collaborate with other renewable energy resources to power a sustainable future.[3] One key factor driving progress in the PV field has been the dedication of PV researchers to high-efficiency solar cells, which drives down CAPEX and manufacturing costs for PV.[4] That is why PV researchers have consistently aimed to design and fabricate increasingly efficient cells.

However, there is a physical limit depending on the number of junctions and the material properties that bounds the maximum achievable efficiency. The current industry is built upon single-junction crystalline silicon cells, as silicon is the second most abundant material on Earth, and it is non-toxic. The practical efficiency limit for single-junction silicon cells, as reported in the literature, is 29.5% ± 0.1%.[5–7] Over the past decades, the PV industry has developed several single-junction Si cell architectures, namely aluminum back surface field (Al-BSF), passivated emitter and rear contacts (PERC), and newer technologies with passivating contacts such as SHJ, TOPCon, POLO, FPC, etc., reaching a record efficiency of 26.81%.[8]

As single-junction efficiency is approaching its practical limit, the industry is currently investigating the viability of double-junction cells for mainstream terrestrial

CONTEXT & SCALE

Does it make sense to design and test solar cells for in-lab standard test conditions (STCs) while they barely experience it during operation? This question is now even more relevant as we have ambitious targets to install solar photovoltaic systems all over the World and also would like to localize solar cell production.

If we do a thorough global and statistical analysis, we will find out that the key design parameters, such as silicon wafer thickness, should be radically different in different parts of the globe. Designing solar cells based on geographical markets not only yields more electrical energy but also is a more resource-efficient and more sustainable practice for a clean energy transition. What is needed to enable this potential is to reach a consensus over the outdoor test conditions (OTCs) that are representative of the atmospheric conditions of different regions of the world, so that the PV cell designs can be optimized based on their location of installation.

© 2024 Elsevier Inc.

applications. The theoretical limit calculated for double-junction two-terminal cells is 45.1%,[9] which we will reevaluate in this work. Despite progress in enhancing the efficiency of PV cells in laboratories, solar cells underperform in outdoor conditions in terms of energy yield. Several pieces of research reported discrepancies between indoor and outdoor performances for various PV technologies such as amorphous, mono- and poly-crystalline silicon, and also perovskites.[10–12] One reason is that the standard test conditions (STCs) differ from real operating environments. Additionally, a crucial link is missing between outdoor performance and solar cell design. There is no effective feedback loop from the field to the lab, or in many cases, the feedback loop is too long to have a meaningful impact on cell design. This means that there are no specific suggestions given about solar cell design based on field performance, yield modeling, or measurement.

At the local or regional scale, numerous research studies have been conducted to evaluate outdoor PV performance indicators.[13,14] These studies typically highlight location dependence and deviations from STC as major contributing factors.[15] Additional factors such as shading, soiling, and aging are also often mentioned. While these research efforts offer valuable insight for local PV engineers regarding PV systems design and installation to maximize electrical yield or minimize the levelized cost of electricity (LCOE), they lack feedback to the PV cell manufacturing industry.

The diversity of potential outdoor working conditions has made it challenging to develop a universally applicable solution. One approach to address this challenge involves utilizing metrics proposed by researchers to classify current PV modules in the market based on test procedures that can effectively represent module performance under outdoor conditions.[16,17] Although such metrics provide feedback at the PV module level, they still fall short of offering guidance for PV cell design. However, this guidance is crucial, as an optimal solar cell design can ensure maximum electricity yield while also optimizing material usage—both pivotal aspects for a sustainable future in the PV sector.

Another proposed solution, which has gained some traction recently, involves the multi-layer mapping of PV-related information through the generation and processing of extensive datasets.[18] Several researchers have created global or regional visualizations of outdoor PV indicators, such as yield,[19] performance ratio,[20] levelized cost/profit of electricity (LCOE/LPOE),[21,22] spectral factor,[23] degradation rate,[24] and (harvesting) efficiency for various single-junction PV technologies—whether monofacial,[20] bifacial, fixed,[25] or tracking.[26] These visualizations have yielded overarching conclusions about PV performance globally and have provided recommendations for PV system design. However, primarily due to the simplifications (such as semi-empirical models[27]) made in such studies, key parameters of a solar cell, e.g., Si wafer thickness, are overlooked, and insights about solar cell design are rarely provided.

In summary, the literature often indicates which technology works better under a specific climate, but it neither optimizes PV technologies for different geographical locations nor provides insights into how cell design can be improved for particular regions or climates. To address this gap, we establish a connection between outdoor performance and solar cell design parameters through detailed yet extensive simulations for all land coordinates on Earth. We then analyzed the results to extract robust highlights that can serve as suggestions for the PV industry. Given that low-cost Si wafers with the necessary lifetime, thickness, and resistivity are indispensable for the PV industry,[28] we particularly focus on these parameters, especially Si wafer

[1]Photovoltaic Materials and Devices (PVMD) Group, Electrical Sustainable Energy (ESE) Department, Electrical Engineering, Mathematics, and Computer Science (EEMCS), Delft University of Technology, Mekelweg 4, 2628 CD Delft, the Netherlands

[2]Lead contact

*Correspondence: h.ziar@tudelft.nl

https://doi.org/10.1016/j.joule.2024.02.023

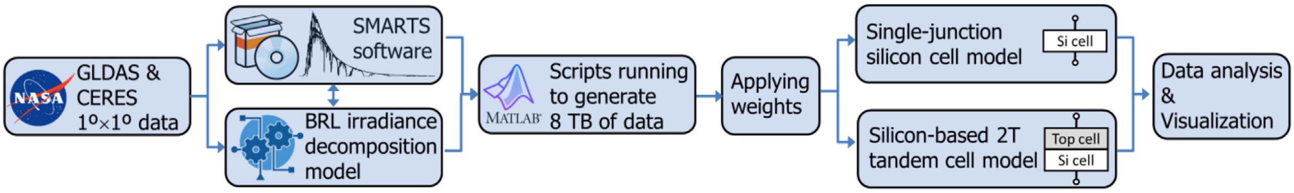

Figure 1. Workflow diagram

Air temperature at the Earth's surface, relative humidity, and surface pressure fetched from NASA's Global Land Data Assimilation System (GLDAS). Precipitable water, snow coverage, ozone total column, aerosol optical depth at 550 nm, surface shortwave down flux, and top-of-atmosphere shortwave flux obtained from NASA's Clouds and the Earth's Radiant Energy System (CERES). Benefiting from SMARTS and BRL models,[31,32] the data were then processed through an automated MATLAB-based platform to generate spectra and ambient temperature for geographical locations. To find appropriate representatives of spectra and temperature for each coordinate, weights were applied. In the next step of the workflow, we optimized the solar cell design for each geographical location. Semiconductor equations were implemented to have one-dimensional solar cell modeling while free carrier absorption (FCA),[33] measured optical properties of silicon as the absorber,[34] incomplete ionization,[35] photon recycling,[5] and band-gap narrowing (BGN)[36] are included. We considered an n-type silicon cell for modeling and the narrow base assumption.[37] The bottom silicon cell of the two-terminal tandem structures was simulated in the same way as the single-junction silicon while the top cell was modeled by implementing detailed balance equations.[38,39] Finally, the outcomes were analyzed and mapped.

thickness. The following sections detail the data collection and preprocessing process, as well as the simulation framework. Furthermore, we present the results and conduct an in-depth investigation. Finally, we highlight the key takeaway messages.

RESULTS AND DISCUSSION

Preparing a competent dataset

We use satellite data sourced from the Global Land Data Assimilation System (GLDAS)[29] and Clouds and Earth's Radiant Energy System (CERES)[30] with 1° × 1° resolution as our primary input. The year 2019 was selected to avoid abrupt atmospheric changes brought about by the COVID-19 pandemic. Subsequently, we input these data into a code that invokes and executes the Simple Model of the Atmospheric Radiative Transfer of Sunshine (SMARTS).[31] SMARTS provides sunlight spectrum data spanning from 280 to 4,000 nm, captured at an hourly resolution. Notably, SMARTS is designed for clear sky conditions. It means that SMARTS does not consider the effect of clouds. To address this limitation, we incorporate the BRL decomposition model[32] to ascertain the ratio between diffuse and direct components of light. The ratios are then employed to adjust the direct and diffuse spectra derived from SMARTS (see supplemental information for more elaboration). The resultant spectra are subsequently transposed on an optimally inclined surface. The optimally inclined surface refers to a *fixed* surface with an azimuth toward the equator and tilted at the same angle as its installation latitude, aligned with previous global-level studies.[19] The selection of 1 year instead of a typical meteorological year (TMY) is because for 1 year, generating hourly sunlight spectra (from 280 to 4,000 nm) for all land locations (1° × 1°) needs 8 TB space for data. Extending it to a time span of at least more than 10 years to represent TMY would have imposed a huge computational and time burden and made the study unworkable.

We have developed an automated software platform and executed the procedure for 15,325 land locations across Earth concurrently on standard office PCs, yielding ~8 TB of data. Figure 1 illustrates the workflow of data preparation and processing, showcasing its linkage with solar cell modeling.

In Figure 2, the distribution of hourly daytime plane-of-array irradiance (G_{PoA}) and PV cell temperature (T_{cell}) is displayed for all global land locations, comprising ~60 million data points. Notably, the STC does not represent the most common working condition of PV cells worldwide.

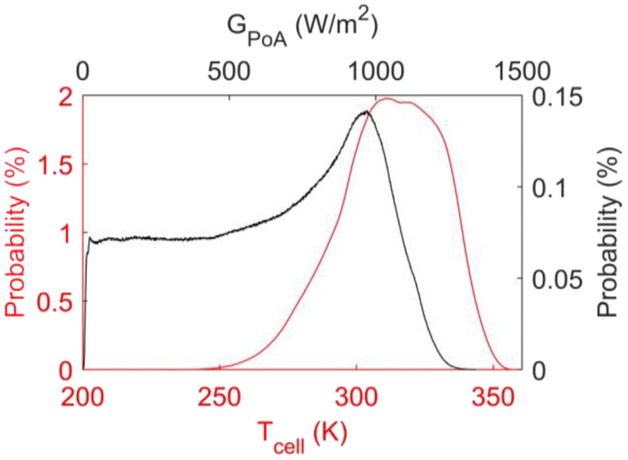

Figure 2. Probability distribution of hourly plane-of-array irradiance and cell temperature for an optimally tilted PV module hypothetically placed on all land locations on Earth. The locations considered have a resolution of 1° × 1°. Only daytime values were considered, and cell temperature was obtained via the nominal operation temperature model, assuming NOCT = 48°C.

Analyzing the hourly distribution of G_{PoA} and T_{cell}, we can infer that the likelihood of STC occurrence is low. However, this does not imply that other potential outdoor working conditions are significantly more frequent than the STC. The core issue lies in the extensive range of working conditions experienced by PV cells. This diversity results in the occurrence chance of STC ±1% being as meager as 0.06%.

Achieving an optimized solar cell design for an extensive array of working conditions is practically unattainable. Conversely, merely optimizing PV cells for STC may lead to suboptimal outdoor performance, wasteful material usage, and missed energy potential, contingent on the geographic location. Hence, we need to establish representative ambient conditions for each specific location. The question arises: what constitutes the most representative outdoor ambient condition? In existing literature, the average value at a site is often chosen. However, this approach introduces a bias because not all the working conditions (irradiance and temperature) hold equal significance for PV systems.

Evidently, to a PV system, a data point characterized by high irradiance and a low temperature has a higher value than a data point featuring low irradiance and high temperature, as the former scenario yields greater energy output. Therefore, a vital step involves assigning appropriate weights to the data points (value-weighted) prior to calculating the average. This process is applied to all hourly data for each geographical coordinate. In this context, we initially assume that PV power exhibits a linear correlation with irradiance (increase) and temperature (decrease). For every location, the highest hourly G_{PoA} observed in the year 2019 is attributed to weight, $w_i = 1$, while the remaining data points are down-weighted linearly as $w_i = G_{PoA}/max(G_{PoA})$. Regarding ambient temperature, we assign the highest weight, $w_i = 1$, to the lowest daytime hourly temperature recorded within the year. Other temperatures are weighted as $w_i = 1 - (T_{amb} - min(T_{amb}))\gamma$, where $\gamma = 0.4\%$ (the temperature coefficient for silicon-based PV). Subsequently, we apply these weights and compute the weighted average for irradiance and temperature at each location. This sets the stage for us to employ semiconductor equations to determine the optimal parameters for silicon PV cells for every geographical coordinate. Figure 3 shows the average and

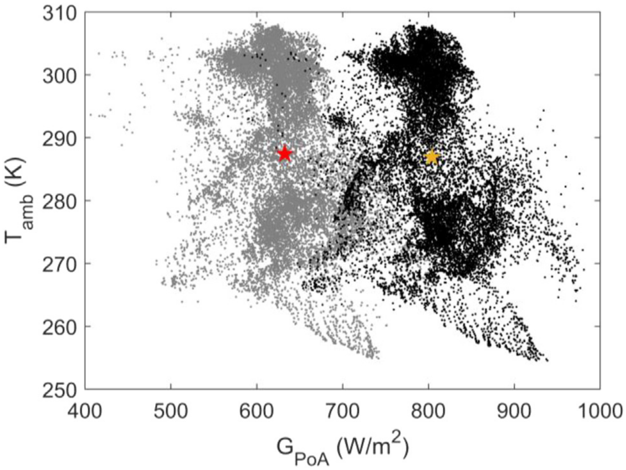

Figure 3. Average (gray) and weighted average (black) values of the plane-of-array irradiance and ambient temperature for 15,325 land locations on Earth. The global average and weighted average of G_{PoA} and T_{amb} are respectively 632.7 W/m^2, 287.4 K, 804.1 W/m^2, and 286.9 K, shown by red and orange pentagrams.

weighted average G_{PoA} and T_{amb} for all Earth locations. As evident, the data cluster shifts toward higher irradiance levels and slightly lower temperatures, aligning with expectations.

Solar cell structures and modeling

We consider two structures: single-junction silicon PV cell and two-terminal X-on-silicon, as shown in Figure 4. Our choice of these structures stems from the following rationale. A plausible scenario is that the single-junction silicon PV will retain as the major player due to its low cost, non-toxic nature, longevity, stability, and the well-established infrastructures that already support it. In this context, tandems will cater to specific needs and applications. This is analogous to the extensive utilization of induction motors (≡ silicon solar cells) across diverse sectors due to their affordability and robustness compared with alternative electric motor topologies (≡ tandem PV cells), which are used mainly for specific applications. On the other hand, alongside economies of scale, efficiency improvement has been one of the key drivers for PV manufacturing cost-effectiveness.[40,41] Hence, an alternative scenario anticipates the PV industry's progression toward enhanced efficiencies and/or reduced manufacturing costs, facilitated by tandem solar cells and/or optimized material usage. In the near to mid-term future, given the industry's heavy reliance on silicon, a shift away from silicon in manufacturing lines and infrastructures appears implausible. Consequently, for double-junction structures, silicon is likely to persist as the bottom cell.[42] However, for configurations with more junctions, envisioning silicon's presence becomes rather difficult because silicon's share in energy generation will drop. In either of the aforementioned scenarios, both single- and double-junction silicon-based technologies are poised to retain substantial significance.[43]

For each geographical location, we optimize the solar cell designs utilizing the input energy spectrum of G_{PoA} and the ambient temperature, thereby obtaining the efficiency of each device. For the silicon solar cell (single-junction or the bottom cell of tandem cell), we implemented one-dimensional semiconductor modeling, whereas for the top cell, we based our calculations on the Shockley-Queisser's approach.[39] Current matching was further used to obtain the overall J-V curve of the two-terminal

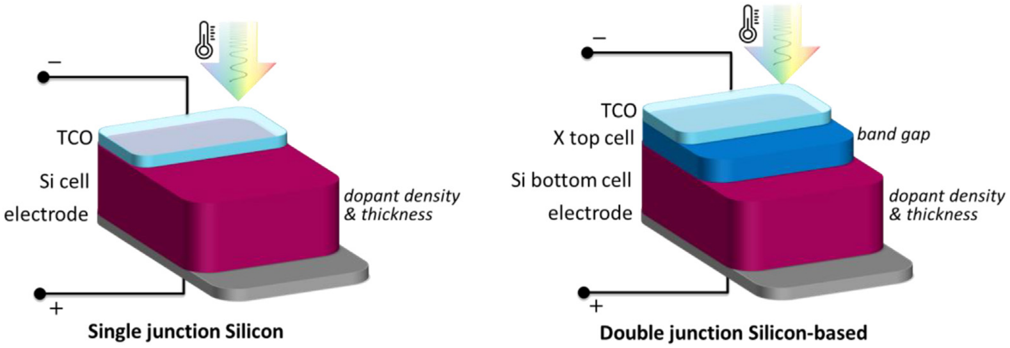

Figure 4. The basic architecture of single-junction silicon solar cell (left) and double-junction two-terminal X-on-silicon solar cell (right) implemented in the simulation framework of this study

The electrode, transparent conductive oxide (TCO), and interface between the sub-cells were considered as perfect. The basic solar cell variables used to optimize the efficiency are written on the right side of each architecture. We considered the dopant density as a design parameter, besides wafer thickness. Therefore, for each geographical location, besides thickness, we varied the based doping concentration. The incoming light spectrum and the ambient temperature depend on the geographical location.

tandem cell. The result of the present simulation framework has been compared with previous works at STC, revealing close agreement. Further elaboration on the present methodology and comparison with previous works can be found respectively in the experimental procedures section and supplemental information.

Global performance of single-junction silicon

To begin, we report our findings for the single-junction silicon cell. Figure 5A displays the maximum achievable efficiency at each geographical location. The average value globally stands at 27.07%. The highest Si cell efficiency (30.6%) on Earth can be reached in the Nunavut territory in Canada while in the Borkou region in Chad, silicon solar cells are not more than 22.4% efficient. We note the variability of design parameters, such as Si wafer thickness, across different locations, with a global average of 112 μm. Parameters for the minimum, maximum, average efficiency, and STC of the Si cell are detailed in Table 1.

We can analyze the values in Table 1 from the perspective of thermodynamic and semiconductor physics. From a thermodynamic perspective, the conversion efficiency of radiation to work follows the Petela-Press-Landsberg efficiency formulation[45–47] and is tightly related to temperature. At higher ambient temperatures, the efficiency drops. That is why in Chad, although being a region with high irradiance, the maximum achievable efficiency is lower than the one in colder climates, such as Canada. From a semiconductor physics perspective, the absorption of silicon increases with temperature.[34] Therefore, at high temperatures, more sunlight is absorbed in the silicon and more photo-generated current is produced. Obviously, more irradiance, aligned with the spectral response of silicon, will cause more photo-generated current. Besides, more intrinsic carrier concentration happens when silicon temperature increases.[48] At the same time, by increasing the quantity of the absorber material (i.e., increasing the thickness of the Si wafer), the photo-generated current increases, but the recombination rate also increases. At some point, the benefit of having thicker silicon (increasing photo-generated current) is compensated by the high recombination rate (drop of the voltage). In hot climates, this optimum point for silicon thickness happens at a lower thickness compared with cold climates. In general, the combined effect of sunlight intensity and spectrum alongside the temperature at a location determines the optimum design parameters for the PV cell in that location, such as its thickness.

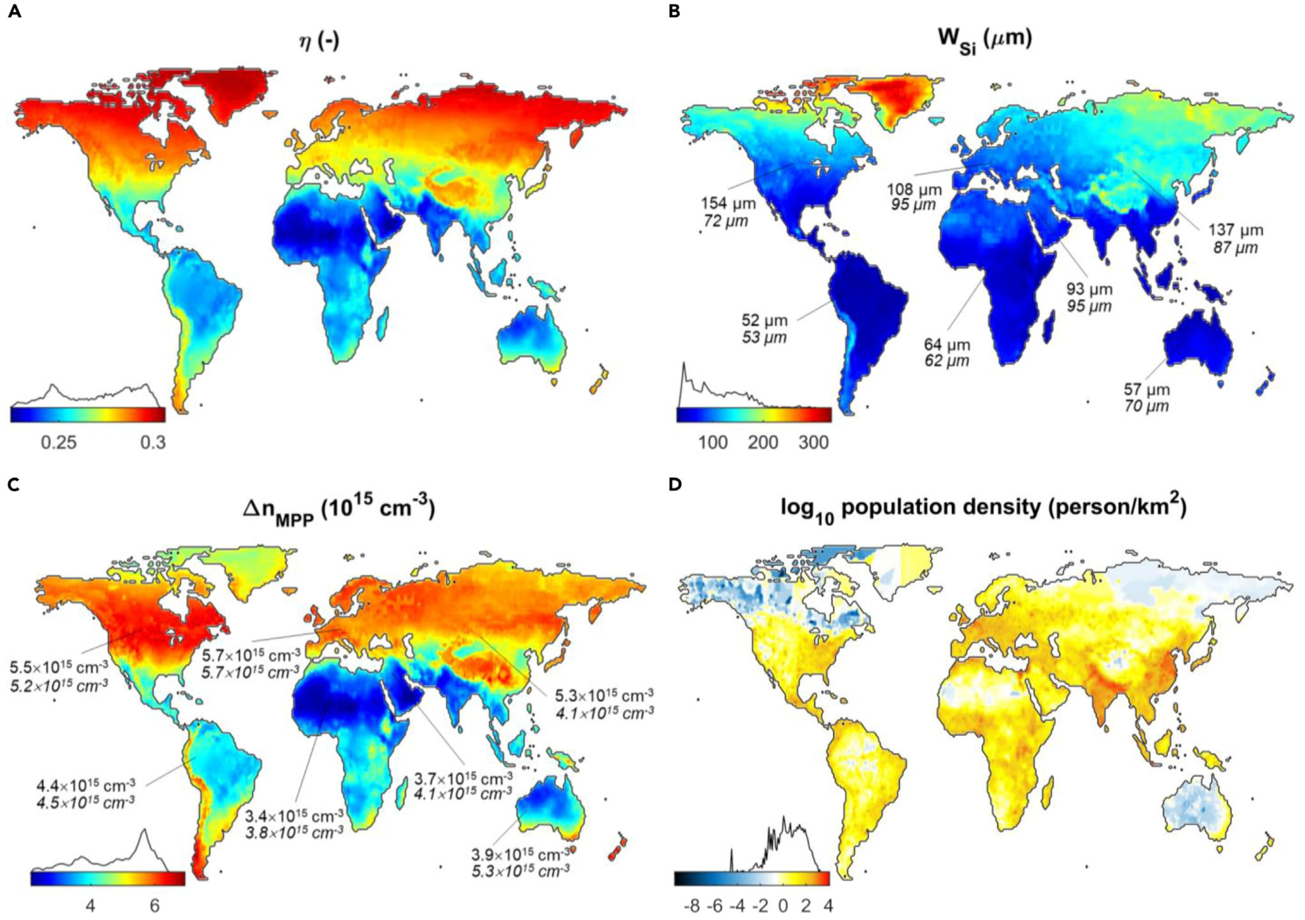

Figure 5. Global plots for single-junction crystalline Si cell and population density

(A) Maximum achievable efficiency of a tilted (with the same angle as its latitude) Si PV cell, optimized for each geographical location.

(B) Corresponding optimum wafer thickness.

(C) Excess carrier concentration (representing injection level) at maximum power point (MPP).

(D) World population density of the year 2020. The data to plot the map were retrieved from Warszawski et al.[44] The color bars are placed on the bottom left of each figure accompanying the color distribution in an arbitrary unit. In (D), a different color bar was chosen and manually tuned for better visual comfort and contrast. In (B) and (C), the optimum Si wafer thickness and injection level for seven geographical markets of North and South America, Europe, Africa, the Middle East, Asia, and Oceania are penned. The top values show the average for that region while the bottom values are weighted average based on the population distribution, shown in (D), over that region.

Wafer thickness, a pivotal design parameter that accounts for up to 50% of current solar cell material costs[49] and used by the PV industry to sustain silicon solar cells economically viable,[50] demonstrates significant dependency on location. Figures 5B and 5C depict the optimum wafer thickness and excess carrier concentration (representative of injection level). We can see that optimum Si thickness radically changes over the globe, whereas all of the optimum cells are in high injection. Maps for effective carrier lifetime and resistivity at MPP are also available in the supplemental information.

In terms of base dopant density, as another design parameter, the optimal designs across all locations consistently hover near the boundary of un-doped silicon (${N_{dop}}^{\pm} \approx 10^{12}$ cm^{-3}), mirroring the scenario at STC. However, the optimum dopant density (n-type cell) very slightly increases $\sim 10^{5}$ cm^{-3} as the Si thickness reduces to 100 μm. Thus, in all locations, the optimum solar cell is a lowly doped wafer. For more details and exact numbers see supplemental information.

Table 1. Silicon solar cell parameters at the highest, average, and lowest efficiencies on the Earth's geographical locations

	η (%)	V_{OC} (mV)	J_{SC} (mA/cm^2)	FF (%)	V_{MPP} (mV)	Δn_{MPP} (cm^{-3})	Δn_{OC} (cm^{-3})	BGN (meV)	$N_{dop}^{\pm}$ (cm^{-3})	ρ_{MPP} (Ω.cm)	L_{MPP}/W (−)	W (μm)
Monofacial												
Maximum	30.63	779	29.62	89.81	716	4.45×10^{15}	1.65×10^{16}	0.047	9.9×10^{11}	0.6674	22.5	275
Average	27.07	728.4	34.52	86.42	652.7	4.82×10^{15}	1.93×10^{16}	0.044	9.9×10^{11}	0.8517	28.1	112
Minimum	22.45	654	32.53	82.44	567	2.15×10^{15}	9.84×10^{15}	0.043	9.9×10^{11}	2.0024	15.7	94
STC	29.65	768.1	43.38	89.00	701.8	7.07×10^{15}	2.57×10^{16}	0.045	9.6×10^{11}	0.4831	34.3	105
Bifacial												
Maximum	30.46	768	39.15	89.63	705	4.24×10^{15}	1.54×10^{16}	0.046	9.9×10^{11}	0.7231	14.9	430
Average	26.68	714.7	36.12	86.30	640	3.84×10^{15}	1.51×10^{16}	0.044	9.9×10^{11}	1.0922	16.3	235
Minimum	22.02	638	32.99	82.21	552	1.65×10^{15}	7.44×10^{15}	0.043	9.9×10^{11}	2.603	8.4	246
STC	29.14	756	43.37	88.89	690	5.62×10^{15}	2.03×10^{16}	0.045	9.9×10^{11}	0.6078	21.7	207

From left to right, parameters are cell efficiency, open-circuit voltage, short-circuit current density, voltage at maximum power point (MPP), excess carrier concentration at MPP and open circuit, band-gap narrowing, dopant density, cell resistivity at MPP, minority carrier diffusion length at MPP over silicon bulk thickness (to check if the narrow base assumption holds), and silicon bulk thickness (as representative of wafer thickness).

Figure 6 shows the distribution of thickness on a global scale, as well as focusing on Europe and Australia. It is evident that the optimal wafer thickness in the European Si PV market is nearly twice that of the Australian market. At high irradiance and temperature, the breakeven point of the increase in the photo-generated current with the decrease in voltage happens at lower thicknesses. Therefore, the optimum thickness in a region such as Australia is lower than in Europe. This observation underscores the importance of tailoring solar cell designs to specific geographic markets. In doing so, we can avoid unnecessary polysilicon wastage and mitigate losses due to excess thickness, resulting in higher voltages and reduced recombination losses. Despite the PV industry's exploration of thinner wafers as a strategy to reduce CAPEX and costs,[51] our results hint toward designing *fitter* single-junction solar cells for geographical markets. Thinner cells may not universally outperform thicker ones, in contrast to studies that solely focus on STC-based solar cell analysis.[40]

The generated data revealed strong correlations between the Si wafer thickness and its resistivity at MPP with the average daytime temperature of Earth's various locations. The relationships can be modeled with simple functions as shown in Figure 7. A noteworthy pattern emerges: in hotter climates, wafer thickness tends to decrease while resistivity experiences an upward trend, and vice versa. The temperature dependence of the optimum thickness of a Si solar cell for a fixed incidence spectrum was well studied in the literature.[52] Here, however, this temperature dependency and its effects were quantified globally under changing sunlight spectra. To cross-validate, the dependency of the absorber thickness at the fixed ASTMG 173 standard spectrum is compared with the work of Engelbrecht and Tiedje,[52] and a very good match was found with slight deviations at high temperatures (above 330 K). For more details, please see supplemental information. On the contrary, we did not uncover such correlations between irradiance and the cell design parameters.

Regarding resistivity, according to Equation 5 in the experimental procedures section, the excess carrier concentration (injection level) at MPP decreases by increasing temperature (in hot climates for cell temperatures above 300 K). Lower carrier concentration means lower conductivity for the photo-generated current and as a result more resistivity.

Estimation on potential polysilicon saving and yield boost

Historically, the polysilicon price can be divided into three time zones: (1) before 2004, there were cycles of oversupply and shortage (pork cycles) as a result of capital

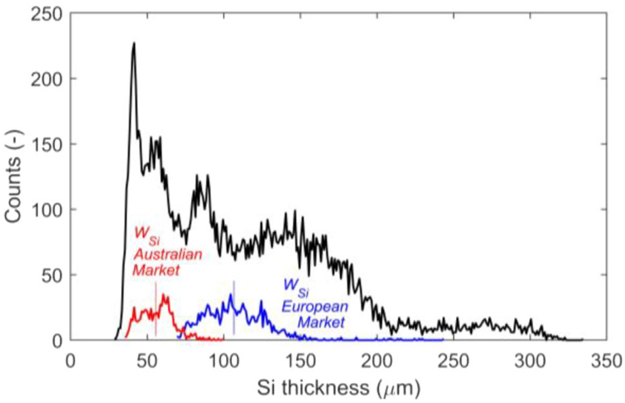

Figure 6. Distribution of optimum Si wafer thickness for the 15,325 geographical Earth locations
The average thickness for Australia is 57 μm (red dotted line) while for Europe, it is 108 μm (blue dotted line).

incentives and long lead times for polysilicon plant development. (2) From 2004 to 2010, a sharp spike in the price as a result of enormous growth in the PV industry happened. (3) After 2010, smoother price rises and falls as a result of the steady and rapid expansion of the polysilicon industry in China. During the second period, and as a result of silicon shortage, the price of polysilicon even went up to ~400 $/kg.[53] A measure taken by the PV industry during that period was to reduce silicon grams per watt through thinner wafers and less kerf loss. As crystalline silicon, the predominant PV technology, approaches its practical limit, and in light of the annual solar PV generation target of ~7,400 TWh for 2030,[54] the necessity for more optimized wafers becomes apparent to further curtail costs and facilitate the widespread deployment of PV systems.

To gauge the potential polysilicon savings, it is essential to identify where PV energy consumption is concentrated. Electrical energy consumption is intricately tied to population density, necessitating the consideration of regional populations due to the higher demand for PV panels in densely populated areas. While industrialized nations tend to consume more electrical energy, for this analysis, we assume an equitable distribution of PV electrical energy consumption per capita globally. Accordingly, we apply population density weighting to the optimal wafer thickness for each geographical region (refer to Figure 5D). The global population-weighted average of the Si wafer is calculated as 80.8 μm. This outcome is influenced by the fact that regions with extreme climates, demanding either very thick or very thin Si wafers, tend to have lower population densities. The ~81 μm is 23% thinner than the thickness at theoretical STC (105 μm) and 50% slimmer than the prevailing industry standard (~160 μm).

We assume hypothetical PV placement across Earth's geographical regions with the same distribution as the population density. Then, we examine two scenarios for comparison of polysilicon consumption per unit of power at cell and module level ($CPP_{cell/module}$), adopting the formulation introduced by Hallam et al.[55]: in scenario 1, we assume optimal single-junction c-Si cell design in laboratory-controlled STCs and its subsequent placement in various Earth locations.

In scenario 2, we envision cell designs customized for each of the seven geographical regions. For both cases, we calculate the polysilicon utilization (CPP) and specific energy yield (Y). We note that, there are constraints with reducing the wafer thickness in

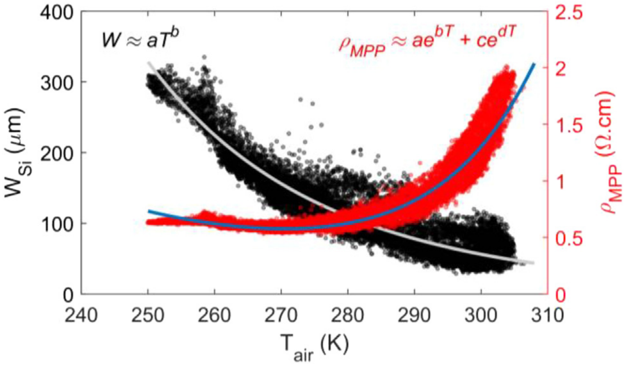

Figure 7. Correlation between the daily air temperature at Earth locations and the cell optimum thickness and resistivity at MPP

Thickness can be approximated by a power function while resistivity can be modeled by a two-term exponential function. In W and ρ functions the coefficients are fixed. For the thickness function the coefficients are $a = 5 \times 10^{25}$ μm/K and $b = -9.67$. For resistivity function the coefficients are $a = 284$ Ω.cm/K, $b = -0.021$, $c = 2.21 \times 10^{-9}$ Ω.cm/K, and $d = 0.067$.

the PV industry, mainly associated with practical difficulties such as handling and kerf loss. We considered such practical constraints through adopting the kerf loss as 43 μm, representing the industrial trend of the kerf loss.[56] Further methodological details are outlined in the experimental procedures section.

Figure 8 shows the annual reduction in polysilicon usage (ΔCPP) and the corresponding increase in specific energy yield (ΔY) resulting from the tailored cell designs for geographical regions, respectively, in kg/kWp and Wh/Wp (and also in percentage values). When cells are designed based on regional environmental conditions, all regions will enjoy more electricity yield and less polysilicon consumption. Even if a single outdoor working condition is chosen as a representation of the global setting, every kW of PV installation annually generates an additional 1.8 kWh while cutting polysilicon consumption by 219 g. Looking at Figure 8, we note that, although the benefit in kWh/kWp is small, the polysilicon savings (g/kWp) is substantial. The saved polysilicon is 16.3% of the overall global consumption. This is only the case when we define one global outdoor working condition. When we design based on regional conditional, the savings will be even more.

In 2022, the global added installed PV capacity was 268 GW, and the polysilicon price was 32.5 $/kg.[57] With this in mind, optimization via outdoor-centric Si wafer design could have potentially conserved ~59 kilotons of polysilicon, equivalent to ~1.9 B$. With a target annual added PV capacity of 650 GW in 2030,[58] and the expected growth, this figure is poised to expand. We acknowledge that in a competitive PV market, one of the comparison metrics is efficiency, assessed under STC. Thus, the prerequisite for rendering the PV market more sustainable and resource-efficient is reaching a consensus on the definition of outdoor test conditions (OTCs).

Suggestion for in-lab tests as representative of outdoor conditions

The most representative outdoor terrestrial working condition for PV cells aligns with scenarios that are more prevalent in regions with higher population densities. Since the definition of OTC must facilitate the design of material-efficient solar cells while maximizing electricity yield, it is imperative that this condition also incorporates value-weighting. Therefore, we apply these two weights of temperature and irradiance (discussed in previous sections) to the ~60 million data points of G_{PoA} and T_{cell}

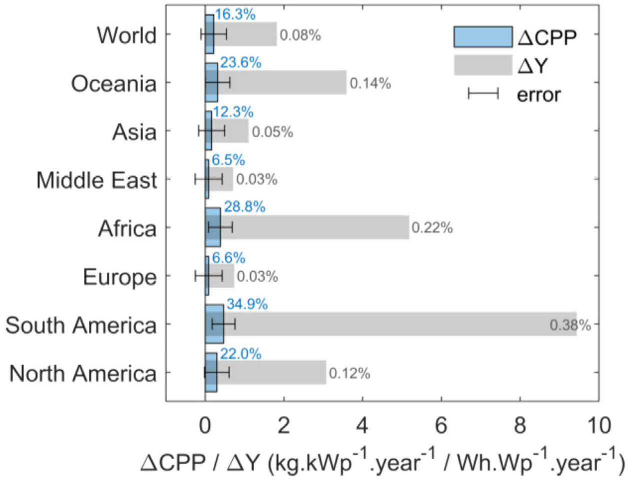

Figure 8. Polysilicon savings and yield increase as a result of designing single-junction c-Si cells based on outdoor conditions for each geographical region

Percentage values are also shown beside each bar with the same color. The optimum design criteria for each geographical region are depicted in Figures 5B and 5C.

shown in Figure 3. The result is G_{PoA} = 757.9 W/m^2 and T_{cell} = 321.8 K. The proposed OTC spectrum is also obtained and plotted in Figure 9. One can see that the difference between OTC and STC spectra diminishes as the wavelength increases. Beyond the statistical derivation of spectra, intensity, and temperature, the pronounced advantage of the suggested test conditions lies in their potential for replication in a laboratory setting. This aspect can substantially mitigate uncertainties, a significant concern in nominal operating cell temperature (NOCT)[59] and nominal module operating temperature (NMOT)[60] test protocols.

Having a recommendation for OTC test conditions, we now move forward to analyzing silicon-based tandem solar cells.

How about bifacials?

The share of bifacial silicon PV cells, which are capable of absorbing light from both sides, is considerably increasing in the market. The market share of bifacial modules with bifacial cells was 30% in 2022.[56] Therefore, before extending this work to tandem solar cells, it is of interest to study bifacial Si solar cells. This section maps the global efficiency of bifacial silicon cell and looks into its optimum thickness through investigating the $W_{Si}^{bifacial} \approx 2 \times W_{Si}^{monofacial}$ proposition of Engelbrecht and Tiedje.[52] We account for the absorption of bifacial silicon and the rear side irradiance and assume a bifaciality factor of one. Similar to the monofacial case, we take the absolute value of the location's latitude as its installation tilt and make use of snow coverage information from NASA's CERES database to incorporate spectrally resolved ground albedo. The details of the modeling approach for bifacial cells can be find the experimental procedures section.

Figures 10A and 10B respectively show the global efficiency and optimum thickness ratio of bifacial versus monofacial cells. At each geographical location, the achievable efficiency of bifacial cells is less than monofacials, which is in line with the reports in the literature at STC.[52] Table 1 summarizes bifacial Si cell parameters at STC besides the highest, average, and lowest efficiencies on the Earth's geographical locations. Comparison of the bifacial cell parameters at STC with the literature is available in the supplemental information.

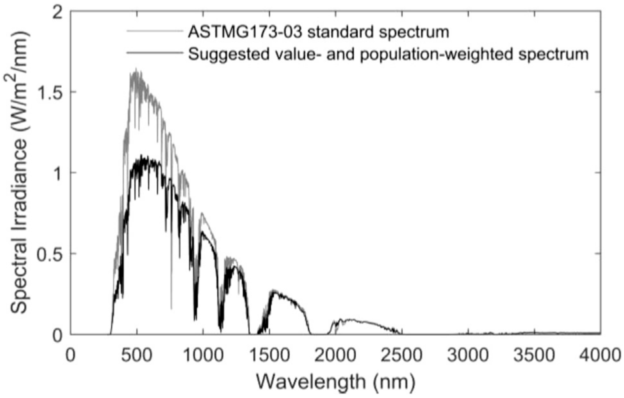

Figure 9. Suggested spectrum for the outdoor representative test

The solar constant of 1,367 W/m^2 was used to be aligned with the guidelines for generating reference spectra.[61] One can adjust the values based on other solar constants, for instance, 1,366.1 or 1,361.1 W/m^2.

Similar to the monofacial Si, the lowest efficiency (22.02%) happens in the Borkou region in Chad. This is due to not only the high temperature but also the low albedo of that region. The highest achievable efficiency (30.46%), however, happens in the North of Greenland, which has a cold climate and high albedo, a favorable situation for bifacial PV cells. The yearly average of daytime ambient temperature and snow coverage maps are presented in the supplemental information file, where one can investigate the correlation of solar cell efficiency with these two parameters over the globe.

While the ratio between the optimum thickness of bifacial to monofacial Si cell stays close to 2 at STC, the ratio ranges from 1.67 to 2.89 globally. To analyze the reason behind the distribution of this ratio globally, we need to recall that the optimum thickness happens when by increasing the wafer thickness the increased photogenerated current (as a result of more absorption) is compensated by the voltage drop (as a result of higher excess carrier density thus more intrinsic carrier recombination dominated by Meitner-Auger recombination mechanism). This breakeven point happens at a thinner thickness under high-temperature and -irradiance conditions. A bifacial cell placed in a high latitude region with frequent snow coverage (i.e., high tilt and high albedo) receives considerable rear side irradiance. This means that the hypothetical bifacial cell works under higher irradiance and temperature compared with its monofacial counterpart installed in the same region. Therefore, its thickness is optimized at lower values and consequently, the $W_{Si}^{\text{bifacial}}/W_{Si}^{\text{monofacial}}$ ratio is lower than 2 in such geographical regions. The opposite is true for low-latitude locations with low snow coverage.

Relation between top-cell band gap and silicon bottom-cell thickness

In numerous instances, the top and bottom cells of tandem solar cells are designed or even optimized separately. However, achieving optimal performance necessitates a holistic design approach that accounts for both top and bottom junctions. This is more important when it comes to two-terminal solar cells. Consequently, physics-based quantified relations between the design parameters of the top and bottom cells can be helpful to designers and cell manufacturers. Two basic design parameters are the band gap of the top cell and the thickness of the silicon wafer for the bottom cell, which are related. To unravel and quantify this intricate relationship, first, we use our simulation platform for the STC, and then, we run it for the

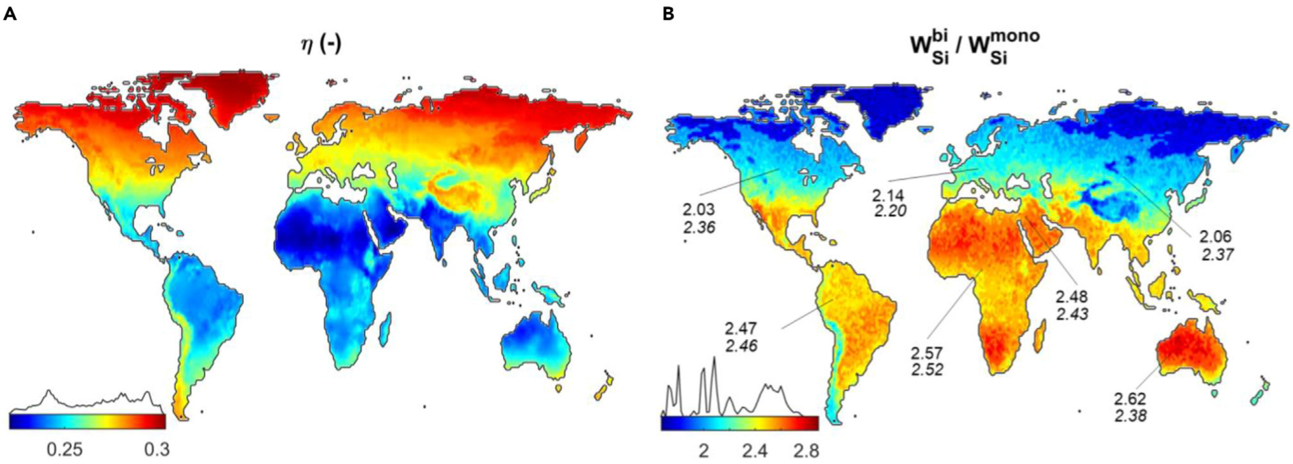

Figure 10. Global plots for single-junction crystalline Si bifacial solar cell

(A) Maximum achievable efficiency optimized for each geographical location.

(B) Corresponding optimum bifacial wafer thickness divided by the optimum thickness of monofacial solar cell. In (B), average (top number) and population-weighted averages (bottom number) are also shown for seven geographical markets.

whole globe. See Figure 15 in the experimental procedures section for the flowchart of simulations for the tandem solar cell, which is a sub-part of the general workflow shown in Figure 1.

The graph in Figure 11 characterizes the interplay between the optimum silicon bottom-cell thickness and the band gap of the top cell. The band-gap range from 0.5 to 2.5 eV is chosen because most of the known photovoltaic materials lie within this range, and lower or above this range the graph does not change. The graph can be divided into three regions. As long as the top-cell band gap is lower than the bottom-cell band gap, all the light is absorbed by the top cell, and thus, no photo-generated current is produced by the bottom cell. Therefore, the thickness of the silicon bottom cell has to be minimized. The second region is where the top-cell band gap exceeds silicon's bottom-cell band gap, where there is a sudden jump to the maximum thickness size (it is defined as 1,000 μm in the simulation). However, this jump happens lower than the silicon band gap because of very minor absorption and thus extremely small J_{SC} near but below the silicon band gap.

The reason is, that although both the top and the bottom cells are active the photo-generated current from the bottom cell is still low and limits the overall tandem cell current. We note that in this region, silicon is still the limiting cell, thus, any increase in its J_{SC} is beneficial to the whole cell. That is why in this region the high recombination rate due to high thickness cannot derate the overall cell efficiency. The third region, however, starts at a band gap that the top cell acts as limiting. Therefore, the thickness of the silicon bottom cell has to drop to provide an adjusted J_{SC} and meanwhile benefits from a lower recombination rate. Within the third region, the maximum efficiency of the two-terminal tandem cell happens while the optimum thickness of silicon bulk is exponentially dropping. As can be seen, at Eg = 1.72 eV, the efficiency is as high as 42.79%, marking the limiting efficiency. This is indeed 2.3% (absolute) lower than the already reported values in the literature.[9] This discrepancy can be attributed to the use of Shockley-Queisser (SQ) calculations in prior works for both cells. The SQ approach, however, disregards Meitner-Auger recombination, leading to inaccuracies, especially when the bottom cell consists of an indirect band-gap material like silicon. Moreover, the previous works did not consider other physical

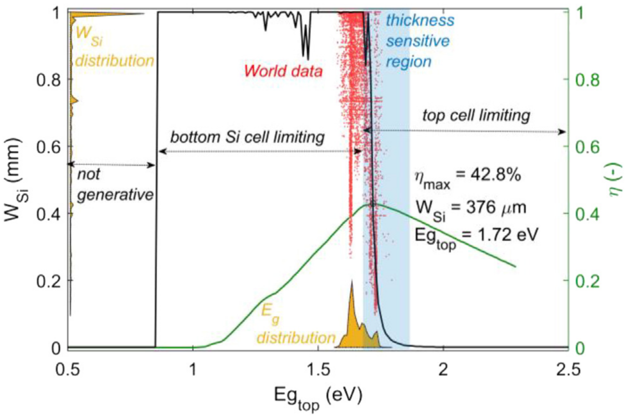

Figure 11. Silicon bottom-cell bulk thickness (n-type) and tandem cell efficiency as a function of the band gap

The efficiency limit and the Si thickness and top-cell band gap at maximum efficiency are also noted. The blue area shows the band gap range where a slight change in efficiency leads to a large change in optimum Si thickness. The red dots show the optimum wafer thickness of the silicon bottom cell for the whole world while the distributions of the W_{Si} and eg_{top} are plotted with orange curves on the vertical and horizontal axes.

phenomena such as free carrier absorption (FCA), measured optical properties of silicon, incomplete ionizations, photon recycling, and band-gap narrowing (BGN). In contrast, our analysis accounts for all these phenomena in the modeling of the bottom silicon cell, reserving the SQ methodology only for the top cell.

Here, we used the step function to model the absorption edge for the top-cell material, in line with the traditional SQ approach and previous literature.[9,62,63] Also, the accuracy of the sole SQ analysis in this work is cross-validated with the work of Rühle,[38] and the result was exactly matching. It is worth mentioning that the two abrupt changes in the W_{Si}-Eg_{top} graph (Figure 11) happen regardless of having soft or hard absoption edges. We investigated that and more details are available in the supplemental information.

Overall, Figure 11 is about theoretically characterizing/plotting the relation between a key feature of the top cell (band gap) and a key feature of the silicon bottom cell (thickness) and pinpointing that the maximum efficiency happens in a region where the thickness change is susceptible to band-gap change or efficiency change. Therefore, we can use this inherent relation between the two cells and design highly efficient tandem cells with less silicon consumption. We observe that the optimal Si wafer thickness in the third region is greatly dependent on the top-cell band gap and overall efficiency ($\boldsymbol{\partial W/\partial E_g}$ and $\boldsymbol{\partial W/\partial \eta}$ are very high). By switching from 1.72 to 1.75 eV, for example, we can lower the required wafer thickness from W_{Si_opt} = 376 µm to $W_{Si\_sub\text{-}opt}$ = 93 µm, meanwhile, the tandem cell efficiency limit drops slightly from 42.8% to 42.4%. The single-junction silicon cells' largest cost component is the Si wafer, and this cost decreases as the wafer is made thinner.[49] Similarly, the thickness of the silicon bottom cell will also play a role in the industry uptake of perovskite-silicon tandem cells.[64] Therefore, future cost-effective tandem cells may be a consequence of suboptimal designs tailored for tandem applications, necessitating *thinner* silicon wafers.

At the maximum efficiency, the top cell absorbs 501.36 W/m^2 from the total 1,000.37 W/m^2 of sunlight power. Therefore, the incoming power is almost equally shared between the two cells; however, the top cell loses 43.3% of its incoming

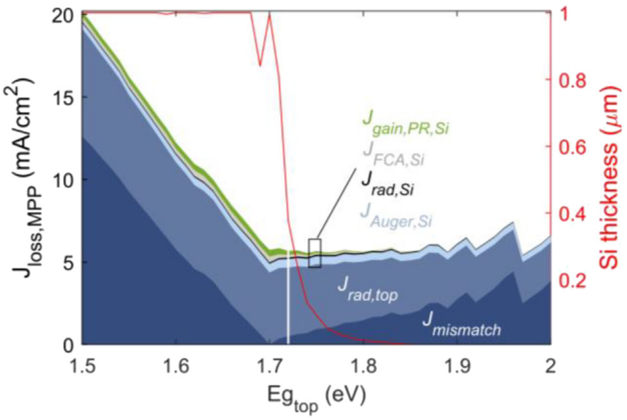

Figure 12. The contribution of current density loss mechanisms in the Si-based tandem cell at the maximum power point with respect to optimum band gap and Si thickness

The white line shows where the maximum efficiency occurs.

power while the Si bottom cell misses 71.2% of the sunlight power that enters into it. The contribution of various loss mechanisms in the Si-based tandem cell at the maximum power point is plotted in Figure 12. It reveals that the maximum efficiency does not coincide with the minimum current mismatch but rather resides slightly away from it. At the peak efficiency, shown with the vertical white line, the highest share of losses belongs to the top-cell radiation recombination ($J_{rad,top}$):

Figure 14 followed by Meitner-Auger recombination of the Si cell ($J_{Auger,Si}$) and the current mismatch between the two cells ($J_{mismatch}$). The current density loss by FCA in bulk silicon ($J_{FCA,Si}$) exerts a more influential role than the radiative recombination in the Si cell ($J_{rad,Si}$). On top of this graph, the current density gain of recycled photons in the Si wafer ($J_{gain,PR,Si}$) is depicted, which fades away by increasing the top-cell band gap (decreasing Si wafer thickness). In aggregate, at the MPP, 20.1% of the photo-generated current is lost through various mechanisms in the two cells.

Global performance of tandem double-junction silicon-based PV

The spectral dependency of solar cells' response to light makes their performance susceptible to variations in incoming sunlight radiation. For the series tandem cells, this susceptibility is high because on one hand the sub-cells have to share the spectrum, and on the other hand, they have to align their output current, which depends on incoming photon flux, to ensure optimum performance.[65] Therefore, we extended our simulations from STC to outdoor conditions, thus optimizing the two-terminal double-junction silicon-based solar cell for the entire world. The thickness and band-gap distributions are displayed on the vertical and horizontal axes with orange hue, and the data points are superimposed on the W_{Si}-Eg_{top} graph of Figure 11 with red dots. As can be observed, the majority of Earth's regions require high thickness (an average of 812 μm), and the band gap that occurs most frequently is at 1.63 ± 0.005 eV (an average of 1.657 eV). Figures 13A and 13D, respectively, visualize the maximum achievable efficiency and the corresponding bottom-cell silicon wafer thickness, excess carrier concentration, and the top-cell band gap. The highest (42.13%) and lowest (34.69%) efficiencies were achieved in the southern part of Chile (Aisén Region) and N'guigmi city in the easternmost part of Niger, close to the Borkou region in Chad, respectively. As can be seen, there is a clear regional reliance on optimum parameters. Similar to single-junction silicon, here, temperature also plays a key role in pinpointing the geographical regions with the highest

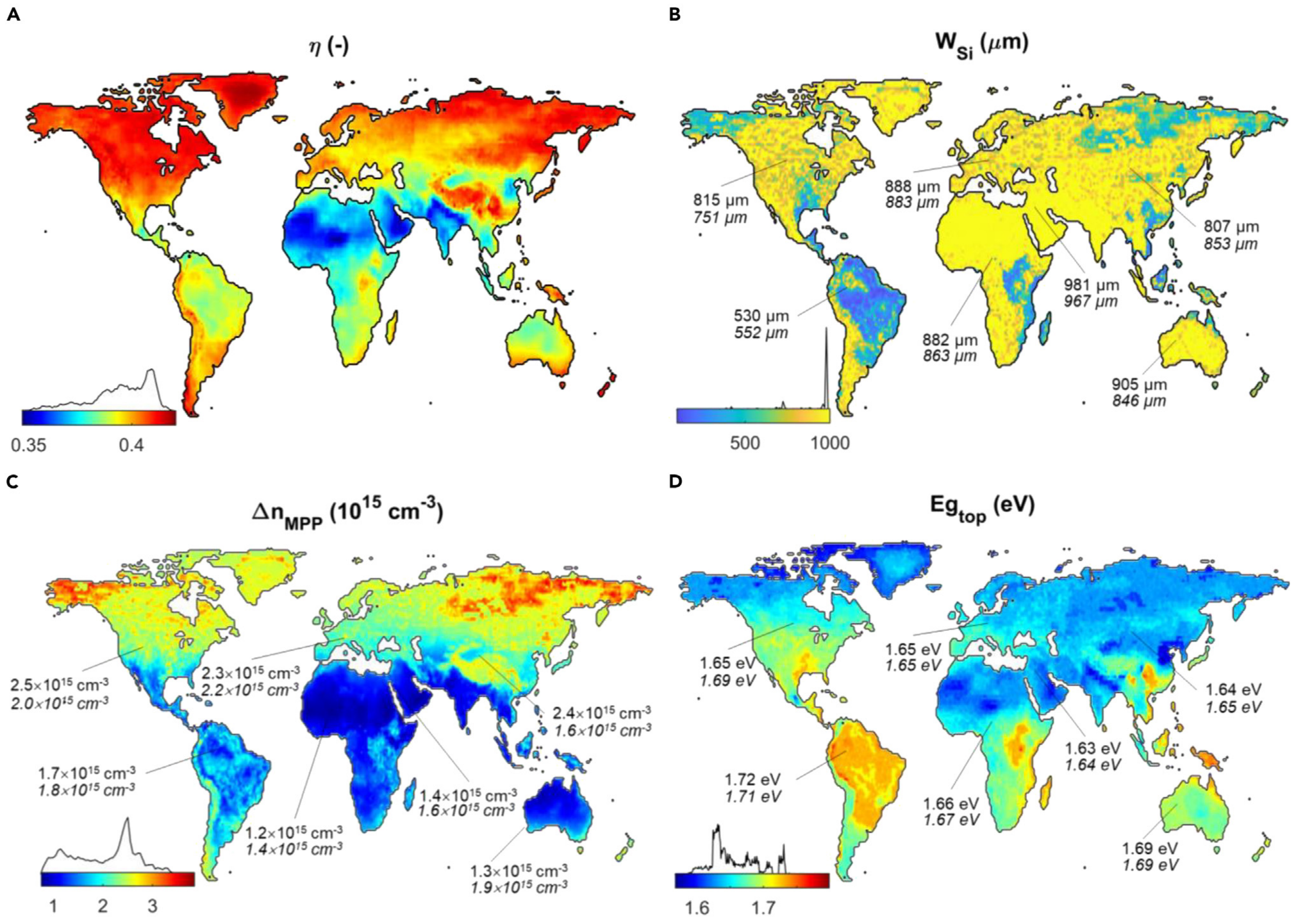

Figure 13. Global plots for double-junction two-terminal crystalline silicon-based cell

(A) Maximum achievable efficiency.

(B) Optimum Si wafer thickness of the bottom cell.

(C) The excess carrier concentration of the bottom-cell Si wafer at MPP.

(D) Optimum material band gap for the top cell. For the three design parameters (thickness and excess carrier concentration of Si bottom cell and the band gap of the top cell) regional average and population-weighted average values are shown on the map. The top values are average, and the values written in italic are weighted average. For better visualization, a different color style was adopted for (B).

and the lowest potential achievable efficiencies. However, the sunlight spectrum is more influential compared with the Si single-junction cell because of the sensitivity of the 2T tandem structure to spectral variations and the need for current matching between the top and bottom cells. The regional average and population-weighted average for bottom-cell wafer thickness, excess carrier concentration, and top-cell band gap are depicted in Figures 13B–13D.

The thickness of silicon wafers obtained for geographical locations is way higher than the current industry standard, implying a more demand for silicon if the PV industry gravitates toward tandem solutions such as perovskite on silicon. However, as shown in the W_{Si}-Eg_{top} graph, suboptimal designs can significantly lower silicon consumption while still ensuring excellent efficiencies. In order to evaluate this on a global scale, we examine the global efficiency of the 2T Si-based tandem solar cells under three scenarios: where the silicon bottom cell has 2/3 and 1/3 of the optimal thickness for that particular location and a scenario where its thickness is fixed at 160 μm (industry standard) for the entire world. Results shown

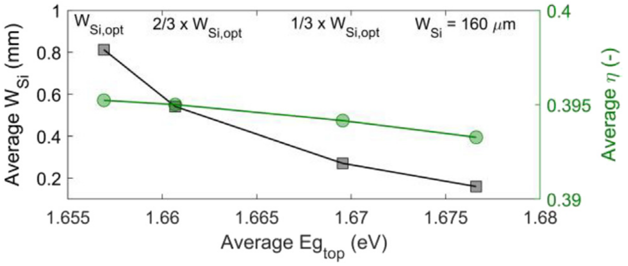

Figure 14. Average silicon wafer thickness, efficiency, and corresponding band-gap values when wafer thickness for each geographical location is reduced to two-thirds of its optimum, one-third of its optimum, and fixed at 160 μm

in Figure 14 demonstrate that the average worldwide efficiency decreases marginally with respect to significant Si wafer thickness reduction, specifically 2.85×10^{-6} 1/μm (~0.3%/mm). In a well-calibrated design, augmenting the top cell's band gap can compensate for the decreased W_{Si}. Figure 14 further showcases how opting for the fixed 160 μm W_{Si} induces, on average, a 0.02 eV increase in the top-cell band gap while only causing a 0.2% absolute drop in the average efficiency.

Discussion and implications for the PV industry

The proliferation of PV technology worldwide is evident but reports highlight that PV cells often fail to achieve optimal performance in outdoor working conditions. Within the solar PV industry and academia, there exists a wealth of resources, data, experience, and techniques, which, if harnessed, could lead to a consensus on global or regional testing requirements to ensure optimum PV performance outdoors. This endeavor would effectively bridge the gap between outdoor performance and solar cell design, while also optimizing the usage of polysilicon, aligning with more sustainable resource utilization.

In this study, we undertook the optimization of both single- and double-junction 2T crystalline silicon-based cells for all terrestrial locations on Earth. Through these detailed simulations and data analysis, we can now address the central question posed by this paper: whether a more conscientious path for the future of silicon-based solar PV lies in deploying *thinner* or *fitter* wafers. We can now construct our response based on two "if" scenarios.

First, should the PV industry continue to heavily rely on single-junction silicon technology, solar cell designs ought to be tailored based on outdoor conditions at global or regional markets. As we showed in the research, a cell with $W_{Si} \approx$ 80 μm operates ideally under outdoor terrestrial conditions, reducing polysilicon usage by 16% (relative to today's industry standard). While ongoing advancements in cell manufacturing may refine the practical application of our statistical findings, the core message remains consistent: *prioritize outdoor optimization over STC*, which solar cells experience only 0.06% of the operational time. Consequently, in this context, the *fitter* option becomes the proposed solution to the posed question.

Second, in the event that silicon-based tandem cells take the lead in the PV industry, suboptimal engineering may be intentionally employed due to the profound sensitivity of silicon wafer thickness to efficiency. This implies that Si wafer thickness can be considerably reduced (even to the current 160 μm industry norm) with a small

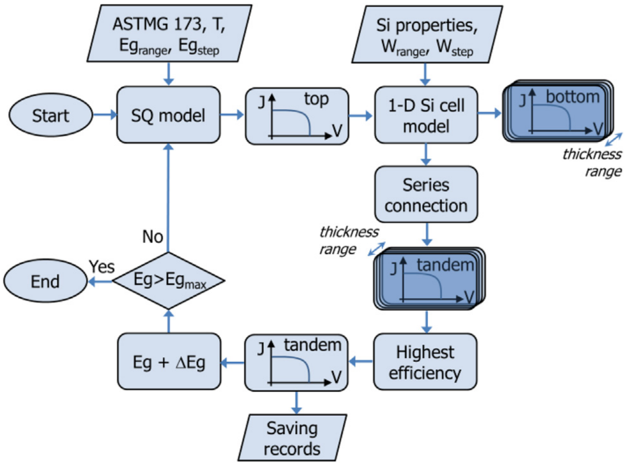

Figure 15. Flowchart of the developed integrated modeling framework for 2T silicon-based tandem solar cell simulations

Note that the input can be any light spectrum and temperature. Here, we put the standard ASTMG spectrum as an example.

impact on efficiency, around 0.3%/mm. Thus, under this scenario, our response to the initial query gravitates toward the *thinner* approach.

We observe that in both scenarios, the amount of polysilicon used per PV electricity generation will decrease, indicating a more sustainable route for the solar sector. Consequently, the pursuit of efficiency enhancements solely under STC conditions ought to give way to a drive for higher energy yield and resource-efficient practices. A key requirement for this transformation is the establishment of regionally or globally accepted OTCs. Such conditions would serve as the foundation upon which PV cells and modules can be designed, manufactured, and evaluated. Through the strategic alignment of solar cell design with diverse global markets, a transformative shift toward a more responsible energy landscape can happen.

EXPERIMENTAL PROCEDURES

Resource availability

Lead contact

Further information and requests for resources should be directed to and will be fulfilled by the lead contact, Hesan Ziar (h.ziar@tudelft.nl).

Materials availability

This study did not generate new unique materials.

Data and code availability

The datasets generated in this study are very bulky (~8 TB) and therefore cannot be made publicly available and are only available from the lead contact on reasonable request. However, the MATLAB codes generated in this study are publicly available at 4TU.ResearchData (https://data.4tu.nl/) under the lead contact's name (Hesan Ziar).

Top-cell modeling based on Shockley-Queisser approach

At every geographical location, we use the G_{PoA} global spectrum and the nominal operating cell temperature (NOCT = 48) model to obtain cell temperature from the ambient data. Then, irradiance and temperature are used as inputs into the SQ limit calculation procedure, clearly explained by Rühle[38]:

$$J_{SC}(E_g) = \int_0^\infty A_{bb}(E)\Phi_U^i(E)dE \qquad \text{(Equation 1)}$$

where J_{SC} is the maximum photo-current density (A m^{-2}) which happens at short-circuit conditions. $E_g = hc/\lambda_g$ is a band-gap energy (eV). $\Phi^i_U = (q\lambda/hc)U^i_\lambda$ is spectral photon flux energy (C m^{-2} s^{-1}), and U^i_λ is the global plane-of-array sunlight spectrum falling on the solar cell (W/m^2/nm). Superscript i denotes the type of radiation (e.g., blackbody or AM1.5g). c is the speed of light (m s^{-1}), and λ is the wavelength of light (m). q is the elementary charge (C). $A_{bb}(E)$ is the ideal absorptance coefficient for band-to-band transition equal to $H(\lambda)$-$H(\lambda$-$\lambda_g)$, where H denotes the Heaviside step function. Not all the photo-generated current can reach the PV cell terminals as a result of recombination. To account for that, radiative recombination current density can be calculated as a function of photon energy (E) and externally applied voltage (V) corresponding to quasi-Fermi level splitting (quasi-Fermi levels assumed flat)[38,66]:

$$J_r(E,V) = 2\pi f_g q \int_0^\infty A_{bb}(E)\frac{E^2}{h^3c^2\left[e^{E-qV/k_BT_C}-1\right]}dE \qquad \text{(Equation 2)}$$

where k_B is Boltzmann constant (J K^{-1}). T_C is solar cell temperature (K) and f_g is the geometrical factor, which is either 1 or 2, respectively when one or both sides of the solar cell emit radiation. A perfect reflector at the solar cell rear side ($f_g = 1$) can slightly increase the efficiency, however, since we are considering this cell as the top-cell we put $f_g = 2$, assuming no reflector is between the two cells. The output current density J of the solar cell can then be written as:

$$J = J_{SC}(E) - J_r(E,V) \qquad \text{(Equation 3)}$$

This equation describes the current-voltage characteristics of the solar cell from which other relevant parameters of voltage at open circuit $V_{OC} = V|_{min|J(V)|}$, voltage at MPP $d(JV)/dJ|_{V=Vmpp} = 0$, current density at maximum power point $J_{mpp} = J_{SC} - J_r(V=V_{mpp})$, maximum power point $P_{mpp} = J_{mpp}V_{mpp}$, and fill factor $FF = P_{mpp}/V_{OC}J_{SC}$ can be obtained. Finally, efficiency of the top cell is obtained by dividing the maximum power point by spectral photon flux energy of incoming radiation: $\eta = P_{mpp}/\Phi^i_U$.

Bottom silicon cell modeling through one-dimensional semiconductor equations

For the silicon bottom cell, as an indirect band-gap material, we extend the model to include non-radiative Meitner-Auger recombination,[67,68] which is the dominant current density loss mechanism.[37] On top of that, free carrier absorption (FCA), measured optical properties of silicon as the absorber, incomplete ionizations, photon recycling, and band-gap narrowing (BGN) are also included to have a comprehensive and more accurate model, whether as the bottom cell or single-junction silicon cell. We assume that the solar cell has no surface or defect recombinations and is equipped with a perfect front anti-reflective coating and a perfect back reflector. These assumptions are aligned with previous studies.[5,69,70] We can rewrite the Equation 3 as:

$$J = J_{SC} - qR_{\text{intr}}W \qquad \text{(Equation 4)}$$

where $R_{intr} = \Delta n/\tau_{intr}$ is intrinsic carrier recombination rate (radiative + Meitner-Auger) and W is silicon solar cell thickness, respectively, with the units of cm^{-3} s^{-1}

and cm. R_{intr} represents how many carriers are recombined per volume in time and it is related to excess carrier concentration Δn and lifetime of carriers in silicon bulk τ_{intr}. To obtain Δn, the solar cell should be modeled as a semiconductor device. We assume thickness of solar cell base is considerably smaller than the average distance a minority carrier can travel before recombining with a majority carrier ($W_B << L_B$), which is known as the narrow base assumption.[37] Then, we apply the one-dimensional calculation procedure described by McIntosh and Altermatt,[71] which considers BGN with Fermi-Dirac statistics.

We implemented the equations for n-type silicon and consider a constant doping profile across the solar cell $N_{dop} = N_D - N_A$, where N_D and N_A are the density of donor and acceptor atoms, respectively (cm^{-3}). The majority carrier density at equilibrium is determined by $n_0 = N_D - N_A = N_{dop}$,which is used as the initial value for the majority and minority carrier densities: $n = N_{dop}$ and $p = n^2_{i0}/N_{dop}$, where n_{i0} is the intrinsic carrier concentration of silicon depending on three fundamental parameters of silicon: band-gap energy as the difference between conduction and valence bands energy $E_{g0} = E_{C0} - E_{V0}$, the density of states at valance and conduction bands N_V and N_C. These parameters are linked via $n^2_{i0} = N_V N_C \exp (E_{g0}/k_B T)$. We considered 3.11×10^{19} and 2.86×10^{19} cm^{-3} for N_V and N_C at 298.15 K, respectively. Temperature dependency of N_V and N_C is modeled by Equations 14 and 15 of Green et al.[72] and temperature dependency of n_{i0} by the work of Misiakos and Tsamakis.[48]

The initial values correspond to the silicon being in equilibrium with no BGN and degeneracy ($\gamma_{BGN} = \gamma_{deg} = 1$). Then we use n, p, N_D, and N_A to calculate the density of ionized donors and acceptors, respectively N_D^+ and N_A^-. We applied Equations 2, 4, 6, and 7 with Table III parameters from the work of Altermatt et al.[73] to obtain N_D^+ and N_A^-. Now we use N_D^+ and N_A^- instead of N_D and N_A in the rest of the calculations. We recalculate our initial values as $n_0 = N_D^+ - N_A^- = N_{dop}^{\pm}$ and $n = N_{dop}^{\pm}$ and $p = n^2_{i0}/N_{dop}^{\pm}$. Having n and p, then valence and conduction bands shifts ΔE_V and ΔE_C along with BGN $\Delta E_g = \Delta E_C - \Delta E_V$ are calculated using Schenk's model.[36]

Here, Fermi-Dirac statistics are used for majority carrier concentration and Boltzmann statistics for minority carrier concentration, as suggested by Altermatt et al.[74] Following this suggestion and the procedure described by Mcintosh and Altermatt,[71] γ_{deg} and γ_{BGN} are then obtained. Further, minority carrier concentration at equilibrium is calculated by $p_0 = n_0 p_0/N_{dop}^{\pm}$. At this point, the following equation was used to calculate the Δn[5]:

$$np = (n_0 + \Delta n)(p_0 + \Delta n) = n_{i0}^2 \exp\left(\frac{\Delta Eg}{k_B T}\right) \exp\left(\frac{qV}{k_B T}\right) \quad \text{(Equation 5)}$$

where $n_{i0} \exp(\Delta E_g/2k_B T)$ is known as effective carrier concentration $n_{i,eff}$. Equation 5 assumes ideal contacts to collect charge carriers which means that quasi-Fermi level separation is equal to the applied voltage, and thus Δn can be obtained as a function of voltage. Finally, n and p are calculated through $n = n_0 + \Delta n$ and $p = p_0 + \Delta n$.

Further, we continue with calculating τ_{intr} using the parametrization developed by Richter et al. in 2012 (Equations 18 and 19 in Richter et al.[75]). The parametrization includes radiative and Coulomb-enhanced Meitner-Auger recombination and has a general form of $\tau_{intr} = \Delta n/[(np - n^2_{i,eff})(C_{n0} g_{eeh} n_0 + C_{p0} g_{ehh} p_0 + C_{\Delta n} \Delta n^{0.92} + B(1 - P_{PR}))]$. C_{n0}, C_{p0}, and $C_{\Delta n}$ are constants while g_{eeh} and g_{ehh} are functions representing procedures in which respectively electron and hole act as the third carrier in Meitner-Auger recombination. B is the rate of radiative recombination and can be expressed as $B_{rel} \times B_{low}(T)$ where $B_{low}(T) = \int B(E,T)dE$ is the radiative recombination coefficient at temperature T for lowly doped silicon formulated by Trupke et al. in 2003[76] and B_{rel} is a relative injection-dependent coefficient developed by Altermatt et al.[77] $B(E,T)$ is written as:

$$B(E,T) = \frac{1}{\pi^2 c^2 \hbar^3 n_{i,eff}^2} n_r^2(E) E^2 \alpha_{bb}(E) \exp\left(-\frac{E}{k_B T}\right) \quad \text{(Equation 6)}$$

where α_{bb} is the absorption coefficient for band-to-band transition and n_r is the refractive index of silicon, both obtained from Green's table of self-consistent optical parameters of intrinsic silicon published in 2008,[34] while considering their temperature dependency. $\hbar = h/2\pi$ is reduced Planck's constant. $P_{PR} = \int A_{bb}(E)B(E,T) dE/\int B(E,T)dE$ is the probability of photon recycling after radiative recombination. So far, we have all the ingredients to calculate R_{intr}. The only remaining parameter is A_{bb}. For the top cell, A_{bb} was formulated ideally using the Heaviside step function, however, for the bottom silicon cell it is defined as:

$$A_{bb}(E) = \frac{\alpha_{bb}(E)}{\alpha_{bb}(E)+\alpha_{FCA}(E)+\frac{j}{4n_r^2 W}} \quad \text{(Equation 7)}$$

where $j = 1$. In case of a bifacial device, the absorption is also given by Equation 7 but with $j = 2$.[52,78] α_{FCA} is a coefficient representing FCA. To calculate α_{FCA} Rüdiger's parametrization of FCA published in 2013 is used.[33] Considering the randomized light-trapping scheme and the isotropic response of the solar cell, the mean path of a light ray inside of the solar cell equals $4n_r^2W$. The chance for creating multiple electron-hole pairs by high energy photons is neglected in Equation 7 because this effect has a minor contribution of <0.1 mA/cm^2.[69] Having Equation 7 in hand, A_{bb} is plugged into Equation 4 to calculate J_{SC} as well. Further, J-V characteristics of the silicon solar cell and finally the parameters of interest can be obtained. Having the J-V curve of the top and bottom cells, we also obtain the overall J-V curve of the two-terminal tandem cell through the algorithmic procedure depicted in Figure 15.

Resistivity ρ of the doped silicon is determined via Arora et al. model[79] of carrier mobility μ and applying $1/\rho = q(n\mu_e + p\mu_h)$. In this case, n and p are calculated while ignoring incomplete ionization because dopant atoms contribute to resistivity independently of ionization. Since n and p are both functions of cell voltage, ρ was calculated only at maximum power point.

Rear side irradiance modeling for bifacial cells

In case of a bifacial cell, we add G^i_λ to the U^i_λ in Equation 1. G^i_λ is the reflected irradiance on the rear side of the cell and is defined as global horizontal irradiance (GHI) multiplied by the spectral albedo times the ground view factor. The spectral albedo is retrieved from SMARTS database of reflectance for two materials of fine snow and lite soil. As long as the yearly average of snow coverage for a geographical region is more than 50%, snow is selected otherwise soil as the material underneath the hypothetical bifacial solar cell. The ground view factor under free horizon condition is obtained by $(1 - \cos\theta)/2$, where θ is the tilt angle of installation.[80]

Polysilicon consumption modeling

The minimum amount of polysilicon per unit of power (CPP) is calculated by knowing the mass of Si wafers, number and efficiency of cells within the module. Since installations are reported based on the nominal power of the modules and the cells might not cover the whole module area, one can write the following equation to calculate CPP at cell and module level in the unit of g/kW[55].

$$CPP_{Cell/Module} = \left(\frac{D_{Si}W}{k_u}\right)\left(\frac{1}{2}\right)\left(\left(\frac{1}{\eta_{cell}} + \frac{A_{cell}n_{cell}}{P_{module}}\right) \pm \left(\frac{1}{\eta_{cell}} - \frac{A_{cell}n_{cell}}{P_{module}}\right)\right)$$

(Equation 8)

where D_{Si} is the silicon density, assumed 2.329 g.cm^{-3}. W is the silicon wafer thickness (cm). To account for the kerf loss, in this work we added k_u as the silicon utilization factor, which is ***W/(W+kerf loss)***. According to latest ITRPV report, for 2022 the average module power for PV plants was 0.407 kW with 108 half-cut M10 cells, which were used to plug in P_{module}, n_{cell}, and A_{cell} in the equation.

SUPPLEMENTAL INFORMATION

Supplemental information can be found online at https://doi.org/10.1016/j.joule.2024.02.023.

ACKNOWLEDGMENTS

The author would like to thank the editorial board of *Joule* and the anonymous reviewers for their professional handling and constructive feedback.

AUTHOR CONTRIBUTIONS

H.Z.: writing – review & editing, writing – original draft, visualization, validation, supervision, software, resources, methodology, investigation, formal analysis, data curation, and conceptualization.

DECLARATION OF INTERESTS

The authors declare no competing interests.

Received: September 9, 2023
Revised: January 15, 2024
Accepted: February 27, 2024
Published: March 18, 2024

REFERENCES

1. Haegel, N.M., Verlinden, P., Victoria, M., Altermatt, P., Atwater, H., Barnes, T., Breyer, C., Case, C., De Wolf, S., Deline, C., et al. (2023). Photovoltaics at multi-terawatt scale: waiting is not an option. Science *380*, 39–42.

2. International; Renewable; Energy Agency (2022). Renewable power generation costs in 2021.

3. Victoria, M., Haegel, N., Peters, I.M., Sinton, R., Jäger-Waldau, A., del Cañizo, C., Breyer, C., Stocks, M., Blakers, A., Kaizuka, I., et al. (2021). Solar photovoltaics is ready to power a sustainable future. Joule *5*, 1041–1056.

4. Kavlak, G., McNerney, J., and Trancik, J.E. (2018). Evaluating the causes of cost reduction in photovoltaic modules. Energy Policy *123*, 700–710.

5. Richter, A., Hermle, M., and Glunz, S.W. (2013). Reassessment of the limiting efficiency for crystalline silicon solar cells. IEEE J. Photovolt. *3*, 1184–1191.

6. Niewelt, T., Steinhauser, B., Richter, A., Veith-Wolf, B., Fell, A., Hammann, B., Grant, N.E., Black, L., Tan, J., Youssef, A., et al. (2022). Reassessment of the intrinsic bulk recombination in crystalline silicon. Sol. Energy Mater. Sol. Cells *235*, 111467.

7. Ziar, H. (2022). Effect of thermal radiation entropy on the outdoor efficiency limit of single-junction silicon solar cells. Sol. Energy Mater. Sol. Cells *242*, 111763.

8. Lin, H., Yang, M., Ru, X., Wang, G., Yin, S., Peng, F., Hong, C., Qu, M., Lu, J., Fang, L., et al. (2023). Silicon heterojunction solar cells with up to 26.81% efficiency achieved by electrically optimized nanocrystalline-silicon hole contact layers. Nat. Energy *8*, 789–799.

9. Futscher, M.H., and Ehrler, B. (2016). Efficiency limit of perovskite/Si tandem solar cells. ACS Energy Lett. *1*, 863–868.

10. Akhmad, K., Kitamura, A., Yamamoto, F., Okamoto, H., Takakura, H., and Hamakawa, Y. (1997). Outdoor performance of amorphous silicon and polycrystalline silicon PV modules. Sol. Energy Mater. Sol. Cells *46*, 209–218.

11. Malik, A.Q., and Damit, S.J.B.H. (2003). Outdoor testing of single crystal silicon solar cells. Renew. Energy *28*, 1433–1445.

12. Tress, W., Domanski, K., Carlsen, B., Agarwalla, A., Alharbi, E.A., Graetzel, M., and Hagfeldt, A. (2019). Performance of perovskite solar cells under simulated temperature-illumination real-world operating conditions. Nat. Energy *4*, 568–574.

13. Srivastava, R., Tiwari, A.N., and Giri, V.K. (2020). An overview on performance of PV plants commissioned at different places in the world. Energy Sustain. Dev. *54*, 51–59.

14. Ishii, T., Otani, K., and Takashima, T. (2011). Effects of solar spectrum and module temperature on outdoor performance of photovoltaic modules in round-robin measurements in Japan. Prog. Photovolt.: Res. Appl. *19*, 141–148.

15. Elibol, E., Özmen, Ö.T., Tutkun, N., and Köysal, O. (2017). Outdoor performance analysis of different PV panel types. Renew. Sustain. Energy Rev. *67*, 651–661.

16. Ziar, H., Asaei, B., Farhangi, S., Korevaar, M., Isabella, O., and Zeman, M. (2017). Quantification of shading tolerability for photovoltaic modules. IEEE J. Photovolt. *7*, 1390–1399.

17. Vogt, M.R., Pilis, G., Zeman, M., Santbergen, R., and Isabella, O. (2023). Developing an energy

rating for bifacial photovoltaic modules. Prog. Photovolt.: Res. Appl. *31*, 1466–1477.

18. Ziar, H., Manganiello, P., Isabella, O., and Zeman, M. (2021). Photovoltatronics: intelligent PV-based devices for energy and information applications. Energy Environ. Sci. *14*, 106–126.
19. Peters, I.M., and Buonassisi, T. (2018). Energy yield limits for single-junction solar cells. Joule *2*, 1160–1170.
20. Peters, I.M., Liu, H., Reindl, T., and Buonassisi, T. (2018). Global prediction of photovoltaic field performance differences using open-source satellite data. Joule *2*, 307–322.
21. Lee, N., Flores-Espino, F., Oliveira, R., Roberts, B., Bowen, T., and Katz, J. (2019). Exploring Renewable Energy Opportunities in Select Southeast Asian Countries: A Geospatial Analysis of the Levelized Cost of Energy of Utility-Scale Wind and Solar Photovoltaics ((National Renewable Energy Laboratory, Office of Energy Efficiency and Renewable Energy)).
22. Yan, J., Yang, Y., Elia Campana, P., and He, J. (2019). City-level analysis of subsidy-free solar photovoltaic electricity price, profits and grid parity in China. Nat. Energy *4*, 709–717.
23. Polo, J., Alonso-Abella, M., Ruiz-Arias, J.A., and Balenzategui, J.L. (2017). Worldwide analysis of spectral factors for seven photovoltaic technologies. Sol. Energy *142*, 194–203.
24. Ascencio-Vásquez, J., Kaaya, I., Brecl, K., Weiss, K.A., and Topič, M. (2019). Global climate data processing and mapping of degradation mechanisms and degradation rates of PV modules. Energies *12*, 4749.
25. Guo, S., Walsh, T.M., and Peters, M. (2013). Vertically mounted bifacial photovoltaic modules: A global analysis. Energy *61*, 447–454.
26. Rodríguez-Gallegos, C.D., Liu, H., Gandhi, O., Singh, J.P., Krishnamurthy, V., Kumar, A., Stein, J.S., Wang, S., Li, L., Reindl, T., and Peters, I.M. (2020). Global techno-economic performance of bifacial and tracking photovoltaic systems. Joule *4*, 1514–1541.
27. Mailoa, J.P., Lee, M., Peters, I.M., Buonassisi, T., Panchula, A., and Weiss, D.N. (2016). Energy-yield prediction for II–VI-based thin-film tandem solar cells. Energy Environ. Sci. *9*, 2644–2653.
28. McIntosh, K.R., Cudzinovic, M.J., Smith, D.D., Mulligan, W.P., and Swanson, R.M. (2003). The choice of silicon wafer for the production of low-cost rear-contact solar cells. In Proceedings of the 3rd World Conference on Photovoltaic Energy Conversion 2003, *60* (IEEE Publications), pp. 2156–2163.
29. Rodell, M., Houser, P.R., Jambor, U., Gottschalck, J., Mitchell, K., Meng, C.-J., Arsenault, K., Cosgrove, B., Radakovich, J., Bosilovich, M., et al. (2004). The global land data assimilation system. Bull. Am. Meteorol. Soc. *85*, 381–394.
30. Wielicki, B.A., Barkstrom, B.R., Harrison, E.F., Lee, R.B., III, Louis Smith, G.L., and Cooper, J.E. (1996). Clouds and the Earth's Radiant Energy System (CERES): an earth observing system experiment. Bull. Am. Meteorol. Soc. *77*, 853–868.
31. Gueymard, C.A. (2005). SMARTS Code, Version 2.9.5 User's Manual (Solar Consulting Services).
32. Ridley, B., Boland, J., and Lauret, P. (2010). Modelling of diffuse solar fraction with multiple predictors. Renew. Energy *35*, 478–483.
33. Rüdiger, M., Greulich, J., Richter, A., and Hermle, M. (2013). Parameterization of free carrier absorption in highly doped silicon for solar cells. IEEE Trans. Electron Devices *60*, 2156–2163.
34. Green, M.A. (2008). Self-consistent optical parameters of intrinsic silicon at 300K including temperature coefficients. Sol. Energy Mater. Sol. Cells *92*, 1305–1310.
35. Altermatt, P.P., Schenk, A., and Heiser, G. (2006). A simulation model for the density of states and for incomplete ionization in crystalline silicon. I. Establishing the model in Si:P. J. Appl. Phys. *100*, 113714.
36. Schenk, A. (1998). Finite-temperature full random-phase approximation model of band gap narrowing for silicon device simulation. J. Appl. Phys. *84*, 3684–3695.
37. Green, M.A. (1984). Limits on the open-circuit voltage and efficiency of silicon solar cells imposed by intrinsic Auger processes. IEEE Trans. Electron Devices *31*, 671–678.
38. Rühle, S. (2016). Tabulated values of the Shockley–Queisser limit for single junction solar cells. Sol. Energy *130*, 139–147.
39. Shockley, W., and Queisser, H.J. (1961). Detailed Balance Limit of Efficiency of p-n Junction Solar Cells. J. Appl. Phys. *32*, 510–519.
40. Liu, Z., Sofia, S.E., Laine, H.S., Woodhouse, M., Wieghold, S., Peters, I.M., and Buonassisi, T. (2020). Revisiting thin silicon for photovoltaics: a technoeconomic perspective. Energy Environ. Sci. *13*, 12–23.
41. Cengiz, M.S., and Mamiş, M.S. (2015). Price-efficiency relationship for photovoltaic systems on a global basis. Int. J. Photoenergy *2015*, 1–12.
42. Green, M.A. (2019). PV technologies, how might these evolve? In Planary Talk at the 36th European Photovoltaic Solar Energy Conference and Exhibition (EUPVSEC) (European Commission).
43. Green, M.A. (2019). Photovoltaic technology and visions for the future. Prog. Energy *1*, 013001.
44. Warszawski, L., Frieler, K., Huber, V., Piontek, F., Serdeczny, O., Zhang, X., Tang, Q., Pan, M., Tang, Y., Tang, Q., et al. (2017). Center for International Earth Science Information Network—CIESIN—Columbia University. Gridded population of the World, version 4, (GPWv4): Population density. In Atlas of Environmental Risks Facing China Under Climate Change, *228* (NASA Socioeconomic Data and Applications Center [SEDAC])).
45. Petela, R. (1964). Exergy of heat radiation. J. Heat Transf. *86*, 187–192.
46. Press, W.H. (1976). Theoretical maximum for energy from direct and diffuse sunlight. Nature *264*, 734–735.
47. Landsberg, P., and Mallinson, J. (1976). Thermodynamic constraints, effective temperatures and solar cells. In International Conference on Solar Electricity, pp. 27–42.
48. Misiakos, K., and Tsamakis, D. (1993). Accurate measurements of the silicon intrinsic carrier density from 78 to 340 K. J. Appl. Phys. *74*, 3293–3297.
49. Louwen, A., Van Sark, W., Schropp, R., and Faaij, A. (2016). A cost roadmap for silicon heterojunction solar cells. Sol. Energy Mater. Sol. Cells *147*, 295–314.
50. Razzaq, A., Allen, T.G., Liu, W., Liu, Z., and De Wolf, S. (2022). Silicon heterojunction solar cells: techno-economic assessment and opportunities. Joule *6*, 514–542.
51. Woodhouse, M.A., Smith, B., Ramdas, A., and Margolis, R.M. (2019). Crystalline Silicon Photovoltaic Module Manufacturing Costs and Sustainable Pricing: 1H 2018 Benchmark and Cost Reduction Road Map (National Renewable Energy Laboratory, Office of Energy Efficiency and Renewable Energy).
52. Engelbrecht, D.A., and Tiedje, T. (2020). Temperature and intensity dependence of the limiting efficiency of silicon solar cells. IEEE J. Photovolt. *11*, 73–84.
53. Bernreuter, J. (2020). Polysilicon price history: A roller-coaster ride from 1981 through 2019 (Bernreuter Research). https://www.bernreuter.com/polysilicon/price-trend/.
54. International Energy Agency (2022). Renewables. https://www.iea.org/energy-system/renewables/solar-pv.
55. Hallam, B., Kim, M., Underwood, R., Drury, S., Wang, L., and Dias, P. (2022). A polysilicon learning curve and the material requirements for broad electrification with photovoltaics by 2050. Sol. RRL *6*, 2200458.
56. (2023). International Technology Roadmap for Photovoltaic (ITRPV) 2022 Results (VDMA Photovoltaic Equipment). https://etip-pv.eu/news/other-news/international-technology-roadmap-for-photovoltaic-itrpv-r-d-findings-from-the-13th-edition/.
57. Shaw, V. (2023). Daqo records average polysilicon price of $32.54/kg in 2022. In PV Magazine. https://www.pv-magazine.com/2023/03/03/daqo-records-average-polysilicon-price-of-32-54-kg-in-2022/.
58. International Energy Agency, IEA (2022). World Energy Outlook 2022.
59. International Electrotechnical Commission (2005). IEC 61215: Crystalline silicon terrestrial photovoltaic (PV) modules–Design qualification and type approval. https://webstore.iec.ch/publication/61346.
60. International Electrotechnical Commission (2016). IEC 61215–2: Terrestrial photovoltaic (PV) modules - Design qualification and type approval - Part 2: Test procedures.
61. (2003). Standard Tables for Reference Solar Spectral Irradiances: Direct Normal and

Hemispherical on 37 Tilted Surface. Book of ASTM Stand. *2012*, 14.

62. Rühle, S. (2017). The detailed balance limit of perovskite/silicon and perovskite/CdTe tandem solar cells. Physica Status Solidi (a) *214*, 1600955.

63. Meillaud, F., Shah, A., Droz, C., Vallat-Sauvain, E., and Miazza, C. (2006). Efficiency limits for single-junction and tandem solar cells. Sol. Energy Mater. Sol. Cells *90*, 2952–2959.

64. Messmer, C., Goraya, B.S., Nold, S., Schulze, P.S.C., Sittinger, V., Schön, J., Goldschmidt, J.C., Bivour, M., Glunz, S.W., and Hermle, M. (2021). The race for the best silicon bottom cell: Efficiency and cost evaluation of perovskite–silicon tandem solar cells. Prog. Photovolt.: Res. Appl. *29*, 744–759.

65. Strandberg, R. (2015). Spectral and temperature sensitivity of area de-coupled tandem modules. In 2015 IEEE 42nd Photovoltaic Specialist Conference (PVSC) (IEEE Publications), pp. 1–6.

66. Wurfel, P. (1982). The chemical potential of radiation. J. Phys. C: Solid State Phys. *15*, 3967–3985.

67. Meitner, L. (1922). Über die entstehung der β-strahl-spektren radioaktiver substanzen. Z. Phys. *9*, 131–144.

68. Auger, P. (1923). Sur les rayons β secondaires produits dans un gaz par des rayons X. C. R. Acad. Sci. *169*.

69. Green, M.A. (1999). Limiting efficiency of bulk and thin-film silicon solar cells in the presence of surface recombination. Prog. Photovolt.: Res. Appl. *7*, 327–330.

70. Kerr, M.J., Cuevas, A., and Campbell, P. (2003). Limiting efficiency of crystalline silicon solar cells due to Coulomb-enhanced Auger recombination. Prog. Photovolt.: Res. Appl. *11*, 97–104.

71. McIntosh, K.R., and Altermatt, P.P. (2010). A freeware 1D emitter model for silicon solar cells. In 35th IEEE Photovoltaic Specialists Conference (IEEE Publications), pp. 2188–2193.

72. Green, M.A. (1990). Intrinsic concentration, effective densities of states, and effective mass in silicon. J. Appl. Phys. *67*, 2944–2954.

73. Altermatt, P.P., Schenk, A., Schmithüsen, B., and Heiser, G. (2006). A simulation model for the density of states and for incomplete ionization in crystalline silicon. II. Investigation of Si:as and Si:B and usage in device simulation. J. Appl. Phys. *100*, 113715.

74. Altermatt, P.P., Schumacher, J.O., Cuevas, A., Kerr, M.J., Glunz, S.W., King, R.R., Heiser, G., and Schenk, A. (2002). Numerical modeling of highly doped Si:P emitters based on Fermi–Dirac statistics and self-consistent material parameters. J. Appl. Phys. *92*, 3187–3197.

75. Richter, A., Glunz, S.W., Werner, F., Schmidt, J., and Cuevas, A. (2012). Improved quantitative description of Auger recombination in crystalline silicon. Phys. Rev. B *86*, 165202.

76. Trupke, T., Green, M.A., Würfel, P., Altermatt, P.P., Wang, A., Zhao, J., and Corkish, R. (2003). Temperature dependence of the radiative recombination coefficient of intrinsic crystalline silicon. J. Appl. Phys. *94*, 4930–4937.

77. Altermatt, P.P., Geelhaar, F., Trupke, T., Dai, X., Neisser, A., and Daub, E. (2005). Injection dependence of spontaneous radiative recombination in c-Si: experiment, theoretical analysis, and simulation. In NUSOD'05 Proceedings of the 5th International Conference on Numerical Simulation of Optoelectronic Devices (IEEE Publications), pp. 47–48.

78. Tiedje, T., Yablonovitch, E., Cody, G.D., and Brooks, B.G. (1984). Limiting efficiency of silicon solar cells. IEEE Trans. Electron Devices *31*, 711–716.

79. Arora, N.D., Hauser, J.R., and Roulston, D.J. (1982). Electron and hole mobilities in silicon as a function of concentration and temperature. IEEE Trans. Electron Devices *29*, 292–295.

80. Smets, A., Jäger, K., Isabella, O., Van Swaaij, R., and Zeman, M. (2016). Solar Energy: The Physics and Engineering of Photovoltaic Conversion, Technologies and Systems (Bloomsbury Publishing).